Journal of Materials Chemistry A

# Single and Dual Metal Atom Catalysts for Enhanced Singlet Oxygen Generation and Oxygen Reduction Reaction

| | |
|---|---|
| Journal: | *Journal of Materials Chemistry A* |
| Manuscript ID | TA-ART-10-2022-008240.R2 |
| Article Type: | Paper |
| Date Submitted by the Author: | 08-Jan-2023 |
| Complete List of Authors: | Tamtaji, Mohsen; Hong Kong University of Science and Technology<br>Wu, Wenting; China University of Petroleum, State Key Laboratory of Heavy Oil Processing, School of Chemical Engineering,<br>Liu, Tongchao; Argonne National Laboratory, Chemical Science and Engineering Division<br>Li, Zhimin; The Hong Kong Polytechnic University<br>Chang, Hsun-Yun; Research Center for Applied Science Academia Sinica,<br>Galligan, Patrick Ryan ; The Hong Kong University of Science and Technology<br>Iida, Shin-ichi; ULVAC-PHI Incorporated,<br>Li, Xiangrong; The Hong Kong University of Science and Technology, Department of Chemical and Biological Engineering<br>Rehman, Faisal; Hong Kong University of Science and Technology School of Engineering, Chemical and biological engineering<br>Amine, Khalil; Argonne National Laboratory,<br>Goddard, William; CALTECH, Beckman Institute, Center for Materials and Molecular Simulation<br>Luo, Zhengtang; Hong Kong University of Science and Technology, Department of Chemical and Biomolecular Engineering,<br>Cai, Songhua; The Hong Kong Polytechnic University |
| | |

# Single and Dual Metal Atom Catalysts for Enhanced Singlet Oxygen Generation and Oxygen Reduction Reaction

*Mohsen Tamtaji[1], Songhhua Cai[2], Wenting Wu[3], Tongchao Liu[4], Zhimin Li[2], Hsun-Yun Chang[5], Patrick Ryan Galligan[1], Shin-ichi Iida[5], Xiangrong Li[1], Faisal Rehman[1,6], Khalil Amine[4*], William A. Goddard III[6*], and Zhengtang Luo[1*]*

[1]Department of Chemical and Biological Engineering, Guangdong-Hong Kong-Macao Joint Laboratory for Intelligent Micro-Nano Optoelectronic Technology, William Mong Institute of Nano Science and Technology, and Hong Kong Branch of Chinese National Engineering Research Center for Tissue Restoration and Reconstruction, The Hong Kong University of Science and Technology, Clear Water Bay, Kowloon, Hong Kong, 999077, P.R. China

[2]Department of Applied Physics, The Hong Kong Polytechnic University, Hunghom, Kowloon 999077, Hong Kong

[3]State Key Laboratory of Heavy Oil Processing, College of Chemistry and Chemical Engineering, Institute of New Energy, China University of Petroleum (East China), Qingdao 266580 (P. R. China)

[4]Chemical Sciences and Engineering Division Argonne National Laboratory 9700 Cass Ave, Lemont, IL 60439, USA

[5]ULVAC-PHI, Inc., Analytical Laboratory, 2500 Hagisono, Chigasaki, Kanagawa 253-8522, Japan

[6]Materials and Process Simulation Center (MSC), MC 139-74, California Institute of Technology, Pasadena CA, 91125, USA

Corresponding authors email: keztluo@ust.hk, amine@anl.gov, and wag@caltech.edu

**Abstract**

We demonstrate rational design of graphene-supported single and dual metal atom catalysts (SACs and DACs) for photocatalytic applications, such as singlet oxygen ($^1O_2$) sensitization and $H_2O_2$ production. Here we combine density functional theory (DFT) and time-dependent DFT (TD-DFT) calculations with experimental verifications. We found a synergistic effect between triplet sensitization and triplet-triplet (Dexter) energy transfer both play a role in the photocatalytic activity through volcano plot of 3d transition metal SACs. More specifically, FeN4-SAC exhibits a low ISC energy gap ($\Delta E_{ISC}$) of 0.039 eV, compared with 0.108 eV for FeNiN8-DACs, both possessing a high Bader charge transfer of 0.366 $e^-$ and 0.405 $e^-$, respectively. Guided by these computational results, we synthesized a series of SACs and a DAC and confirmed their structures with scanning transmission electron microscopy (STEM) along with X-ray absorption near-edge structure (XANES) and extended X-ray absorption fine structure (EXAFS). We then confirm their band structures with low-energy inverse photoemission spectroscopy (LEIPS) and UV-Vis-NIR. Subsequently, we synthesized the catalysts for photooxygenation of anthracene and two-electron oxygen reduction reaction (ORR) to measure their photocatalytic activity. We found that $H_2O_2$ production through two-electron ORR competes with the $^1O_2$ generation through Dexter energy transfer. FeN4-SAC demonstrates a high photooxygenation conversion of 86% and a high $^1O_2$ quantum yield of 1.04, obtained from ESR spectroscopy, while low $H_2O_2$ production. On the contrary, NiN4-SAC exhibits a low $^1O_2$ generation and a high $H_2O_2$ production mainly because of the high Gibbs free energy of OOH* intermediate. This work proposes an effective DFT-guided strategy for designing SACs and DACs for various photocatalytic applications.

**Keywords:** DFT, TD-DFT, photocatalyst, Bader charge transfer, Intersystem crossing, ML

## Introduction

With maximized utilization of metallic atoms, single atom catalysts (SACs) and dual atom catalysts (DACs) exhibit high activity and selectivity.[1] By introducing atomically dispersed metal atoms, the electronic and excitation structures can be tuned for appropriate exciton and charge transfer towards desired applications.[2] Previous studies have devoted tremendous efforts to SACs for various electrochemical reactions.[3–10] However, the application of SACs and DACs for photochemical reactions such as $^1O_2$ sensitization, $CO_2$ reduction reaction ($CO_2$RR), oxygen reduction reaction (ORR), hydrogen evolution reaction (HER), $N_2$ reduction reaction (NRR), and photoinduced electron/energy transfer reversible addition-fragmentation chain transfer (PET-RAFT) polymerization has rarely been reported.[11,12] More specifically, $^1O_2$ sensitization can be used for organic synthesis, wastewater treatment, and photodynamic therapy (PDT). In order to apply SACs and DACs for the aforementioned applications, the mechanism of exciton, charge, and energy transfer in the SACs and the synergistic effect of the two metal atoms in DACs requires fundamental studies to bring insights into their rational design.[13]

Density functional theory (DFT) provides a powerful tool to calculate the electronic structure and Bader charge transfer ability of SACs in their ground state. As an example, the Bader charge transfer between dioxygen ($O_2$) and graphene-supported FeN4-SAC, CoN4-SAC, NiN4-SAC, and CuN4-SAC is investigated through DFT calculations, finding that FeN4-SAC induces more Bader charge transfer. This leads to selective and enhanced singlet oxygen ($^1O_2$) sensitization, which is used for the PDT of tumor cells.[14] Moreover, charge transfer between DACs and dioxygen is investigated using DFT calculations, finding the importance of magnetic coupling on the performance of DACs.[15] In addition to studying the charge transfer using DFT calculations, the electronic structure of materials in their excited states can be examined using time-dependent DFT

(TD-DFT) calculations to provide additional fundamental insights into the photocatalytic process.[16] For instance, TD-DFT calculations is used to calculate the singlet and triplet excitons of CoN4-SAC and N-doped graphene,[17] showing that by introducing atomically dispersed Co metals, the ISC energy gap lowers to 0.06 eV, compared to 0.367 eV for the N-doped graphene.[17] Nevertheless, the screening of all the 3d transition metals in terms of charge transfer and ISC energy gap is needed through DFT and TD-DFT calculations to discover the best combination for SACs and DACs.

Machine Learning (ML) provides a fast, inexpensive, accurate, and supportive tool to extract complex structure-activity relationships and to perform feature engineering in large parameter space, such as the type of SAC and coordination environment.[18–21] In fact, ML combined with time-consuming and computationally expensive DFT calculations, provides a new direction for the rapid and low-cost rational design of SACs for optimal electrochemical and photochemical catalytic activities.[22–24] For example, several studies have used ML to perform feature importance analysis and design SACs and DACs with excellent activity by predicting the Gibbs free energy ($\Delta G$) of reaction intermediates for $CO_2$RR, ORR, HER, and NRR.[25–27]

In this work, we examine the performance of MN4-SACs and FeNiN8-DAC, where M stands for all the 3d transition metals, towards photocatalytic $^1O_2$ sensitization and $H_2O_2$ production. We use TD-DFT calculations to examine the energy levels of singlet and triplet excitons and to calculate the ISC energy gap while using DFT to calculate the charge transfer to explain the triplet-triplet (Dexter) energy transfer process. Inspired by the volcano plot obtained from theoretical calculations, we synthesized SACs and a DAC using the pyrolysis approach. The local atomic structure of SAC and DACs and their local surroundings is confirmed using X-ray photoelectron spectroscopy (XPS), X-ray absorption near-edge structure (XANES), and extended X-ray

absorption fine structure (EXAFS). The bandgap structures are revealed using Low Energy Inverse Photoemission Spectroscopy (LEIPS) and UV-Vis spectroscopy. To evaluate the $^1O_2$ generation ability of catalysts, we used photooxygenation reactions and ESR measurements, while the $H_2O_2$ production is measured using the $KMnO_4$ titration method. We conclude that FeN4-SAC shows superior performance for $^1O_2$ generation, with a quantum yield of 1.04 due to higher triplet sensitization and triplet-triplet energy transfer. On the other hand, NiN4-SAC exhibits higher $H_2O_2$ production due to lower electron-hole recombination and a higher Gibbs free energy of the OOH* intermediate ($\Delta G_{OOH*}$, obtained from ML). Our results indicate that the DFT- and TD-DFT-guided design of SACs enables accelerated discovery for desired photochemical activities, providing a new tool for their rational design.

## Experimental section

### Chemicals

An ethanol solution of 96% is obtained from the Merck Inc. of Germany. Anthracene of ≥ 99.0% is purchased from the Fluka Co. Acetonitrile (ACN) of ≥ 99.9% is obtained from the Scharlab Company, China. $KMnO_4$, $H_2SO_4$ (95%), acrylamide (AM, 99%), hydrochloric acid (HCl 37%), $FeCl_3$•$6H_2O$ (97%), $CoCl_2$•$6H_2O$ (99%), $NiCl_2$•$6H_2O$ (98%), 2,2,6,6-Tetramethylpiperidine (TEMP, 99%), and potassium hydroxide (KOH, 99%) are all obtained from Sigma Inc. USA. Graphite (grafguard) is used with an average particle size of 350 mm. Ultrapure (18.2 MΩ) deionized water (DI) is used for washing purposes during the whole synthesis process. All chemicals mentioned above are used as received and utilized with no further treatments.

### Synthesis of graphene oxide (GO)

GO is synthesized using the modified hummers method through the exfoliation and oxidation of expanded graphite sheets during thermal treatment.[28] Briefly, microwave-expanded graphite (1 g)

is dispersed into 30 ml of $H_2SO_4$ (98%) inside a 500 ml round bottom flask, followed by stirring in an ice bath. After a duration of 2 hours, 5 g of $KMnO_4$ is slowly added to the suspension. Subsequently, the suspension is kept stirring at room temperature for 4 hours until the color became pale brownish. Then, the solution is slowly diluted with 50 ml of deionized (DI) water while the color change towards brown. After that, the solution is diluted with 200 ml of DI water while stirring for another 2 hours at room temperature. Finally, enough amount of $H_2O_2$ (30 wt.%) is added dropwise to the solution mixture to reduce the residual $KMnO_4$ until the solution's color is converted into bright green. The solution is stirred for another 2 hours and then allowed to settle for 1 day. The synthesized GO is then centrifuged and washed at least 9 times with DI water at 15000 rpm for 30 min. The centrifuged GO solution ultimately reaches a concentration of 8 mg/ml concentration by dispersing into DI water for further experiments.

**Synthesis of SACs**

Different types of catalysts supported by graphene are synthesized, namely, FeN4-SAC, CoN4-SAC, NiN4-SAC, and FeNiN8-DAC, along with nitrogen-doped graphene (N-doped). Metal precursors, $FeCl_3 \cdot 6H_2O$, $CoCl_2 \cdot 6H_2O$, and $NiCl_2 \cdot 6H_2O$ salts are dissolved to make 0.05 M solution of $Fe^{3+}$, $Co^{2+}$, and $Ni^{2+}$ respectively.[29,30] GO suspension is diluted by mixing 12.5 ml of 8 mg/ml GO into 120 ml DI water. 250 µl of 0.05 M of $Fe^{3+}$, $Co^{2+}$, or $Ni^{2+}$ solution and 1.2 ml of acrylamides (25 wt.%, as a nitrogen precursor) are added into the diluted GO suspension and stirred for 23 hours. The mixed solution is freeze-dried for four days and went through a two-step annealing process, as follows, to synthesize highly dispersed SACs.[31] The brownish freeze-dried sample went through the first annealing step in a 1-inch quartz tube furnace at 300 ℃ for 3 hours under Ar (202 s.c.c.m). Then the blackish sample is washed using $H_2SO_4$ (0.05 M) and ethanol (96%) several times before being freeze-dried. Subsequently, the freeze-dried sample went through a second annealing process at 500 ℃ for 3 hours under Ar (202 s.c.c.m) to produce FeN4-SAC,

CoN4-SAC, and NiN4-SAC. Similarly, FeNiN8-DAC is prepared using 125 µl of each $Fe^{3+}$ and $Ni^{2+}$ solution as the metal precursors in the procedure mentioned above. The control sample (N-doped) is prepared without adding a metal precursor.

**Photocatalytic activity**

The photooxygenation of anthracene is performed to measure the photocatalytic activity of N-doped, FeN4-SAC, CoN4-SAC, NiN4-SAC, and FeNiN8-DAC towards $^1O_2$ generation. The photooxygenation reactions are performed using a 125 ml two-neck flask connected to an oxygen balloon to add oxygen to the reaction, at room temperature and atmospheric pressure. A warm white LED light (20 W) is positioned beside the flask. In a typical procedure, 5 mg of as-prepared SACs is added to the reactor containing 0.5 mg of anthracene and 0.5 µl of cyclohexanone as the internal standard dissolved in 5 ml of acetonitrile. After 1 hour of constant stirring at 500 rpm, 50 µl of the sample is centrifuged and injected for GC analysis. In addition, the solution is titrated with $KMnO_4$ (5 mM) to measure the amount of produced $H_2O_2$.

**Characterization and analysis**

The structure and morphology of synthesized DAC and SACs are examined by transmission electron microscopy (TEM, JEOL JEM 100CXII) and scanning electron microscopy (SEM, JEOL JSM-7800F). The coordination of single metal atoms at the atomic level resolution is investigated using scanning transmission electron microscopy (STEM, ThermoFisher Spectra 300). Chemical structure verification, elemental composition, and elemental bonding states are extracted from X-ray photoelectron spectroscopy (XPS, PHI *VersaProbe* III). All XPS spectra are corrected concerning the C 1s peak (284.48 eV). Energy dispersive X-ray analysis (EDX, JEOL JEM 100CXII, and JEOL JSM-7800F) is used for the elemental mapping. The Fe-K, Co-K, and Ni-K edge is acquired through the synchrotron radiation-based XAFS facility at Argonne Photon Source

(APS) to provide the local environment around metal atoms through the X-ray Absorption Spectroscopy (XAS). The bandgap and conduction band of samples are measured using UV-vis-NIR absorption spectra (PerkinElmer Lambda 20) and Low Energy Inverse Photoemission Spectroscopy (LEIPS, PHI *VersaProbe* III), respectively. SACs are then analyzed using XRD (PANalytical) and Raman (Renishaw Raman RM3000 scopes with a 514 nm laser source). Electron spin resonance (ESR) spectra (JEOL JES FA200 spectrometer at 9.8 GHz X-band with 100 Hz field modulation) are recorded at room temperature to measure the $^1O_2$ generation. The conversion of reactions is calculated based on the GC-MS (Thermo Fisher GCMSD, ISQ QD, EI) technique.

**DFT and TD-DFT calculations**

Our density functional theory (DFT) calculations used the Becke 3-parameter, Lee, Yang, and Parr (B3LYP) hybrid functional 6-31G (d,p)[32,33] basis set for ground-state optimizations and charge transfer calculations.[17,34,35] In addition, we calculated the energy levels of the singlet and triplet excitons using time-dependent DFT (TD-DFT) to examine the photoexcitation process, based on the optimized ground-state geometry. Previous studies have shown that B3LYP can accurately describe the excited states and adsorption energies (charge transfer) of reaction intermediates in similar metal complexes.[36–39] Therefore, we believe that the B3LYP hybrid functional can accurately describe both the excitons and charge transfers. We also applied the B3LYP-D3 method to include van der Waals attraction (London dispersion) interactions.[40] All the DFT calculations are performed using Gaussian 09 software, and visualizations are performed using GaussView 6.0.16 and Multiwfn 3.8.[41,42]

**Machine Learning (ML) for Gibbs free energy calculation**

We use Support Vector Regression (SVR) as a supervised machine learning (ML) algorithm to calculate the Gibbs free energy of various intermediates using the results from the DFT calculations. The reason for applying the ML algorithm is to show the potential application of this technique for the fast and accurate prediction of Gibbs free energies for all transition metal SACs on N- and O-doped graphene- and porphyrin-based substrates. We use scikit-learn, numpy, matplotlib, rdkit, mendeleev, pickle, and bayes_opt libraries in Python 3.6 to process the data and train the ML algorithm (available free of charge).[43] The dataset contains 2084 DFT-predicted Gibbs free energy values for H*, OH*, O*, OOH*, COOH*, CO*, CHO*, and COH* intermediates of electro- and photochemical $CO_2$RR, ORR, and HER. The training data distribution for each intermediate is displayed through violin and box plots in **Figure S31** to show the probability density of the dataset at different values. The input features used in our ML models include the properties of metal atoms, substrates, and intermediates. By introducing the properties of intermediates, the ML is generalized for different reaction intermediates. In addition, by introducing the properties of metal atoms and substrates, the ML model is applicable for all the transition metals and graphene- and porphyrin-based substrates with N and O dopants. For the training of ML algorithms, all the input features are normalized between 0 and 1, while the data is partitioned into the training set (90%) and the test set (10%). $R^2$-score and the mean absolute error (MAE) are used to evaluate the performance of the ML algorithm.[44] As shown in **Figure S33a**, the $R^2$-scores for the train and test set are 0.930 and 0.891, respectively. In addition, the MAE values for the train and test set are 0.11 eV and 0.18 eV, respectively. The ML algorithms are trained for the minimum MAE without any signs of underfitting and overfitting. In addition, the bayes_opt library (Bayesian optimization) is used to optimize the hyperparameters of the SVR

algorithm and increase the accuracy of the results. For more details, please see the Supporting Information.

## Results and discussion

Singlet oxygen ($^1O_2$) generation from high quantum yield materials such as single and dual metal single atom catalysts (SACs and DACs) provide one of the most effective technologies for further photodynamic therapy (PDT), wastewater treatment, and organic synthesis applications.[44,45] As shown in **Scheme 1**, the $^1O_2$ sensitization process possesses an intersystem crossing (ISC) energy transfer ($S_1 \xrightarrow{k_{ISC}} T_1$) with a subsequent triplet-triplet energy transfer between $T_1$ and $^3O_2$ via a Dexter multielectron transfer process ($T_1 + {}^3O_2 \xrightarrow{k_{Dexter}} S_0 + {}^1O_2$).[44,46] According to the Arrhenius equation (please see section S6 of Supporting Information for more details), the rate of ISC energy transfer ($k_{ISC} \propto \exp(-\Delta E_{ISC}/kT)$) reaches its maximum when the ISC energy gap ($\Delta E_{ISC}$) is close to zero. This leads to a high concentration of $T_1$, which is critical for many photochemical reactions such as $CO_2$RR, ORR, HER, and PET-RAFT polymerization.[47–52] Also, according to the Dexter equation ($k_{Dexter} \propto \exp(-2R/L)$), a lower $O_2$-SAC distance (R) leads to a higher triplet-triplet energy transfer from $T_1$ to $^3O_2$. Therefore, to rationally design appropriate SACs and DACs for photocatalytic applications, a systematic study on ISC energy transfer and charge transfer ability of SACs and DACs is of importance.

This study performs DFT and TD-DFT calculations to investigate the Dexter and ISC energy transfers, respectively. The structure of understudied N-doped, MN4-SAC, FeNiN8-DAC, and FeNiN6-DAC, are shown in **Figure S22**, where M stands for all the 3d transition metals. The ground state geometries are optimized using the B3LYP flavor of the DFT method with the 6-31G (d,p) basis set. Subsequently, the energy levels of the singlet and triplet excitons are calculated

using TD-DFT. **Figure S24** displays the schematic Jablonski diagram for the synthesized samples showing the singlet ($S_1$, $S_2$, and $S_3$) and triplet ($T_1$ and $T_2$) excitons based on ground-state ($S_0$) with oscillator strengths ($f$) and primary electronic components of excitons in **Table S2**. The intersystem crossing energy gap ($\Delta E_{ISC}$) is calculated based on the difference between energy levels of singlet and triplet excitons ($\Delta E_{ISC}=S_1-T_2$), which are shown through a volcano plot in **Figure 1a**. The results in **Figure 1a** indicate that the presence of metal atoms can lower the $\Delta E_{ISC}$, to enhance triplet ($T_1$) sensitization, compared to the N-doped sample ($\Delta E_{ISC}$=0.367 eV). In addition, the FeN4-SAC possesses smaller $\Delta E_{ISC}$ compared to other samples, resulting in a higher rate of ISC ($K_{ISC} \propto \exp(-\Delta E_{ISC}/kT)$). **Figure S23** shows the frontier molecular orbitals involved in $S_0 \rightarrow S_1$ excitation of FeN4-SAC with the primary electronic component of HOMO→LUMO, indicating the charge transfer from ligand to metal. The triplet excitations of FeN4-SAC are composed of $S_0 \rightarrow T_2$ and $S_0 \rightarrow T_1$ transitions with the primary electronic components of HOMO-2 →LUMO and HOMO→LUMO, respectively.

DFT calculations were performed to calculate the electron transfer between MN4-SACs or FeNiN8-DAC and $O_2$ providing in-depth insights into the mechanism of $^1O_2$ generation through Dexter energy transfer. **Figure 1b** shows the Bader charge transfer from catalysts to $O_2$, exhibiting an exponential decrease versus their distance ($K_{Dexter} \propto \exp(-2R/L)$, where L is the van der Waals radius of the SAC, and R is the distance between dioxygen and SACs obtained from DFT calculations, (**Figure S26**). **Table S3** displays the SAC-$O_2$ distance (R), the Bader charge transfer, and the O-O bond length which suggests that transferred electrons occupy the half-filled antibonding $\pi_x^*$ and $\pi_y^*$ orbitals, giving rise to a distinct spin-flip degree for dioxygen that elongates its bond length.[53] As shown in **Table S3**, distinct charge transfers of 0.405 $e^-$ result in elongating the O-O bond from 1.205 Å for the ground state of dioxygen to 1.305 Å in dioxygen

adsorbed on FeNiN8-DAC. The inset of **Figure 1b** shows charge transfer from FeN4-SAC to $O_2$ during adsorption, indicating a high Bader charge transfer. The charge transfer from other SACs to $O_2$ during adsorption is shown in **Figure S27**.

Based on the above calculations, we synthesized FeN4-SAC, CoN4-SAC, NiN4-SAC, FeNiN8-DAC, and N-doped graphene samples. The chemical states and compositions of the prepared samples are studied with X-ray photoelectron spectroscopy (XPS). **Figures S1-S4** show the wide range XPS spectra for all the synthesized samples. The XPS results show a tiny peak for metals, with Fe, Co, and Ni metal contents to be 0.33, 0.31, and 0.37 wt.% in the synthesized FeN4-SAC, CoN4-SAC, and NiN4-SACs samples, respectively. Also, we found Fe and Ni metal contents to be, respectively, 0.19 and 0.18 wt.% in the synthesized FeNiN8-DAC sample. To identify different types of nitrogen in the SACs, we deconvoluted the N 1s peak, suggesting different types of nitrogen for FeN4-SAC, CoN4-SAC, NiN4-SAC, and FeNiN8-DAC, and N-doped samples. For example, **Figure S2b** shows that the N 1s peak for FeN4-SAC deconvoluted into pyridinic-N (398.2 eV), Fe-N (398.8 eV), pyrrolic-N (400.2 eV), and oxidized-N (407.1 eV).[29] **Figure 2a-c** shows a high-resolution peak spectrum for Fe, Co, and Ni metals of synthesized samples, indicating that Fe, Co, and Ni metals existed in the catalysts with two valence states ($p_{1/2}$ and $p_{3/2}$) compared to their pure and oxide states. The binding energy of Fe $2p_{3/2}$ in FeNiN8-DAC shifts by -0.3 eV compared with that in FeN4-SAC, suggesting a lower valence state for Fe, while there is no shift in the Ni $2p_{3/2}$. This is in agreement with the Mulliken charge analysis of Fe, changing from 1.07 $e^-$ to 0.89 $e^-$, respectively, in FeN4-SAC and FeNiN8-DAC, suggesting that the N and Ni atoms donate partial electrons to Fe atom (Figure 2b).[54]

The electronic states and atomic configuration of the single metal atoms in the synthesized samples are further investigated with the XANES and EXAFS. **Figure 3a-c** represent the metal K-edge

XANES spectra for FeN4-SAC, NiN4-SAC, FeNiN8-DAC, and CoN4-SAC, indicating that the local atomic structure around Fe, Co, and Ni metal atoms is distinct from their bulk metals. This is more clearly observed from its first derivative curves (**Figure S8**), suggesting intermediate oxidation states for SACs. **Figure 3a-c** indicates a blueshift in the absorption edge of SACs compared to their bulk metals, suggesting their valence state is higher than 0. The higher valence state should be attributed to the coordination between metal (M) and N forming FeN4, CoN4, and NiN4 coordination.[29,30,55] Moreover, three peaks for Fe atom in **Figure 3a** are pointed with A, B, and C representing 1s→3d, 1s→$4p_z$, and 1s→$4p_{xy}$ transitions, multiple scattering.[30,55] The differences in intensity of the peak C as the main edge peak in **Figure 3a** is confirmed by the existence of divacancy-based M-N4C4 moieties bonded axially with broken D4h symmetry.[29] In addition, a downshift in the main peak C of K-edge XANES spectra of FeNiN8-DAC compared to FeN4-SAC is observed, suggesting the delocalization of unpaired electrons in the high-lying $d_{z2}$ orbital of Fe into ligands,[56] more clearly shown through the spin density in **Figure S29**. In addition, as shown in the inset of **Figure 3a**, Fe K-edge XANES spectra of FeNiN8-DAC shows a red-shift adsorption edge compared to FeN4-SAC, indicating the decreased valence of Fe in FeNiN8-DAC [54], in agreement with XPS results. The red-shift in the Fe K-edge XANES spectra can be obtained from theory using the accurate finite difference (FD) approach implemented in the FDMNES software,[29] shown in **Figure S9**.

In addition, the bonding and coordination environment around metal in the SACs are further studied with the EXAFS Fourier transform (FT) for all four SACs shown in **Figure 3d–f**. **Figure 3d** shows that the EXAFS FT spectra of FeN4-SAC and FeNiN8-DAC samples exhibit primary peaks corresponding to Fe-N bonding at around 1.42 Å, different from Fe-O peak at 1.55 Å[57] and Fe-Fe peaks at 2.17 and 4.48 Å. **Figure 3e** also shows EXAFS FT spectra for NiN4-SAC and

FeNiN8-DAC samples exhibit a primary peak attributed to Ni-N bonding at 1.45 Å, different from Ni-O peak at 1.62 Å[58] and Ni-Ni peaks at 2.17 and 4.19 Å. Similarly, **Figure 3f** shows EXAFS FT spectra for CoN4-SAC sample exhibiting a primary peak attributed to Co-N at 1.35 Å, different from the Co-O peak at 1.63 Å[58] and Co-Co peaks at 2.15 and 4.20 Å.

The surface structure, morphology, and elemental mapping of FeN4-SAC are confirmed by SEM images. **Figure S11** shows the SEM imaging and EDX elemental mapping for Fe, C, and N elements, confirming the presence of all elements in the synthesized FeN4-SAC sample. **Figure 4a** and **Figure S13** show TEM images for the FeN4-SAC sample, suggesting the uniform dispersion of the Fe metal atoms without noticeable aggregations. **Figure S14** shows TEM imaging and EDX elemental mapping of the FeNiN8-DAC sample for C, N, O, Fe, and Ni elements, confirming the presence and ideal dispersion of individual Fe and Ni metal atoms in the synthesized FeNiN8-DAC sample. The results are consistent with an XRD spectrum provided in **Figure S7** for N-doped, FeN4-SAC, CoN4-SAC, NiN4-SAC, and FeNiN8-DAC samples. The XRD spectra occupy only one broad graphitic carbon peak (002) at 24.1°. No other peak is detected that would correspond to metal species or their compounds with oxides or nitrides.[29]

As shown in **Figure S6**, the intensity ratio of D/G-band ($I_D/I_G$) in the Raman spectra increases from 0.714 for graphene oxide (GO) to 0.867 for the FeN4-SAC sample, indicating the increase in the density of defect vacancies ($n_D$, please see Supporting Information for more details).[59] The Raman results are consistent with the STEM image of the FeN4-SAC sample, shown in **Figure 4b**, indicating rich porous support. ADF-STEM further examined the atomic structure of SACs. **Figure 4c-f** shows the STEM images of FeN4-SAC, CoN4-SAC, NiN4-SAC, and FeNiN8-DAC samples, where the atomic form of metals (white dots) distributes homogeneously throughout the whole graphene support.

As shown in **Figure S18**, UV-Vis spectra of N-doped, FeN4-SAC, CoN4-SAC, NiN4-SAC, and FeNiN8-DAC samples exhibit higher light-harvesting ability in the ultraviolet range (π-π* transition) and relatively weaker absorbance in the visible range. In order to find the optical bandgap (Eg) of samples, we obtain the Tauc plot from the UV-Vis spectra for each sample (please see section S3 of Supporting Information for more details).[60] As shown in **Figure S19**, the Eg values are 1.90, 2.35, 2.38, 2.53, and 2.27 eV, respectively, for N-doped, FeN4-SAC, CoN4-SAC, NiN4-SAC, and FeNiN8-DAC samples. The efficient bandgap of NiN4-SAC suggests its low electron-hole recombination rate (see equation S6 of Supporting Information for more details).[61] In addition, we observed that introducing metal atoms increases the bandgap energy compared to the N-doped sample, in agreement with literature [62]. We attribute the increase in the bandgap to a decrease in planarity of the framework due to the presence of the metal atom leading to less delocalization of unpaired electrons.[63,64]

We further carried out Low Energy Inverse Photoemission Spectroscopy (LEIPS)[65,66] experiments to measure the conduction band (CB) levels (relative to vacuum level) for N-doped, FeN4-SAC, CoN4-SAC, NiN4-SAC, and FeNiN8-DAC samples, (**Figure S21**). As shown in **Figure 6a**, the valence band (VB) levels in SACs are then calculated by adding the Eg values derived from Tauc plots to the CB levels.[64] The CB and VB levels increase as metal atoms are introduced, indicating the contribution of metal atom d orbitals to the conduction and valence bands, which is consistent with PDOS obtained from DFT calculations (**Figure S28**). We emphasize here that introducing metal atoms can enable alignment of the CB and VB, which is of fundamental importance to achieve a favorable position of the edges of the CB and VB with respect to the target redox species.[61] This also is of great importance to achieve efficient charge carrier separation, reduce electron-hole recombination, and improve photoactivity.[61]

Furthermore, we examined the photocatalytic activity of the prepared SACs to verify our computational results. **Figure 5a** shows the reaction conversion of photooxygenation of anthracene (displayed in the inset) for N-doped, FeN4-SAC, CoN4-SAC, NiN4-SAC, and FeNiN8-DAC, indicating that FeN4-SAC has the highest reaction conversion. This result is further confirmed by electron spin resonance (ESR) of SACs upon irradiation for 10 min in the presence of 2,2,6,6-Tetramethylpiperidine (TEMP), as shown in **Figure 5b**. **Figure S16** also shows ESR spectra of N-doped, FeN4-SAC, CoN4-SAC, NiN4-SAC, FeNiN8-DAC, and methylene blue (MB, as the reference) without irradiation (dark) and with irradiations for 5 and 10 minutes in the presence of TEMP. The $^1O_2$ trapping-ESR tests are performed by mixing samples and TEMP (0.01 M) in deionized water to measure the $^1O_2$ generation ability. As shown in **Figure 5b** and **Figure S16**, the ESR spectra clearly display a 1:1:1 triplet signal with a g-value of 2.002, which is characteristic of 2,2,6,6-tetramethylpiperidine-N-oxyl (TEMPO). Amongst all the synthesized SACs, FeN4-SAC shows the highest ESR peaks, implying more $^1O_2$ generation. Inspired by the ESR measurements, the $^1O_2$ quantum yield of all samples is calculated based on the $^1O_2$ quantum yield of methylene blue (please see section S2 of Supporting Information for more details). As shown in **Figure 5a**, FeN4-SAC displays a high $^1O_2$ quantum yield of 1.04, while N-doped shows a low $^1O_2$ quantum yield of 0.26, indicating that introduction of the metal centers is critical for $^1O_2$ generation. This also agrees with our TD-DFT and DFT calculations results shown in **Figure 1**, which indicate that FeN4-SAC at the summit of the volcano plot with a low $\Delta E_{ISC}$ and a high charge transfer. It is worth mentioning that based on the calculations shown in **Figure 1**, MnN4-SAC and CrN4-SAC also possess low ISC energy gap and high Bader charge transfer which might lead to their high $^1O_2$ generation, similar to FeN4-SAC, and should be experimentally investigated by the community.

Considering the results from TD-DFT and DFT calculations, we may find the rate of $^1O_2$ sensitization based on the ISC energy gap ($\Delta E_{ISC}$) and distance between SAC and $O_2$ (R) (see section S6 of Supporting Information for more details):

$$K_{1_{O_2}} = k_{Dexter}^{\alpha} k_{ISC}^{\beta} \propto \exp\left(-\alpha\frac{\Delta E_{ISC}}{kT} - \beta\frac{2R}{L}\right) \quad (2)$$

in which α and β are constants, k is the Boltzmann constant, T is the temperature (in K), and L is the van der Waals radius. Equation 2 implies that $^1O_2$ generation depends simultaneously on both the triplet sensitization and the charge transfer processes. **Figure 5c** displays experimental $^1O_2$ quantum yield versus $\exp(-\alpha\Delta E_{ISC}/kT - 2\beta R/L)$, suggesting the following descriptor for the rational design of single and dual atom photocatalysts:

$$K_{1_{O_2}} = 2.64 \times \exp\left(0.10\left(-\frac{\Delta E_{ISC}}{kT} - \frac{2R}{L}\right)\right) \quad (3)$$

This descriptor explains the exponential relationship of experimentally measured quantum yields with theoretically calculated $\Delta E_{ISC}$ and R, indicating that the lower $\Delta E_{ISC}$ and the lower R for FeN4-SAC favors a higher $^1O_2$ generation than for the other systems. This equation also suggests that in order to design single and dual atom photocatalysts, one should consider the synergistic interplay between triplet sensitization (ISC energy gap) and triplet-triplet energy transfer (metal complex-$O_2$ charge transfer). Moreover, this descriptor can be extended to all the photocatalytic reactions such as ORR, $CO_2$RR, HER, and PET-RAFT polymerization. To do that, the Dexter energy transfer and R should be calculated using DFT calculations for the specific reaction.

In addition to $^1O_2$, the electron transfer through redox reactions can generate $H_2O_2$ or reactive oxygen species (ROS), including $O_2^{\cdot-}$ and ·OH, which would compete with Dexter energy transfer for $^1O_2$ sensitization, which should be considered.[67] Based on the following reaction mechanism,

the two-electron oxygen reduction reaction (ORR) can compete with Dexter energy transfer to produce $H_2O_2$ rather than $^1O_2$:[68,69]

$$* + O_2 + e^- \rightarrow {}^*O_2^{\bullet -} \quad (4)$$

$${}^*O_2^{\bullet -} \rightarrow {}^1O_2 + e^- \quad (5)$$

$${}^*O_2^- + H^+ \rightarrow OOH^* \quad (6)$$

$$OOH^* + e^- + H^+ \rightarrow H_2O_2 \quad (7)$$

Therefore, we measured the amount of $H_2O_2$ produced during the photocatalytic reaction. The reaction mixtures for FeN4-SAC, CoN4-SAC, and NiN4-SAC are titrated with the 5 mM $KMnO_4$ solution to measure the amount of $H_2O_2$ produced.[70] **Figure 6c** shows the results for $H_2O_2$ production for various SACs, indicating a very small concentration of $H_2O_2$ produced and the selective nature of SACs to produce $^1O_2$ compared to $H_2O_2$.[17] In addition, NiN4-SAC exhibits more $H_2O_2$ production than FeN4-SAC and CoN4-SAC due to three main reasons including (i) its low quantum yield of $^1O_2$ sensitization as the competitive reaction, (ii) its efficient bandgap energy, and (iii) its higher Gibbs free energy of the OOH* intermediate. To some extent, as shown in **Figure 6b**, the larger bandgap of NiN4-SAC, obtained from the Tauc plot in **Figure 6a**, suggests its low electron-hole recombination rate and can explain its higher $H_2O_2$ production.[68,71,72] In addition, based on **Figure 6d**, the higher Gibbs free energy of the OOH* intermediate ($\Delta G_{OOH*}$), predicted from the machine learning (ML) technique, further explains the increased $H_2O_2$ production for NiN4-SAC. Indeed, the higher $\Delta G_{OOH*}$ for NiN4-SAC represents the weaker binding energy for OOH* intermediate, making the desorption of the OOH* intermediate more favorable and lowering the overpotential towards $H_2O_2$ production.[73] This agrees with the theoretically obtained volcano plot in the recent work indicating that $\Delta G_{OOH*}$ of 0.429 eV for

NiN4-SAC leads to the optimal adsorption/desorption of the OOH* intermediate for $H_2O_2$ production.[74]

## Conclusion

We combined density functional theory (DFT) and time-dependent DFT (TD-DFT) calculations to rationally design single and dual atom catalysts (SACs and DACs) for photocatalytic application. These theoretical investigations show a synergistic effect of triplet sensitization and triplet-triplet energy transfer that explains that FeN4-SAC is best because it has a low ISC energy gap ($\Delta E_{ISC}$) of 0.039 eV and a high Bader charge transfer of 0.366 $e^-$. Inspired by these results we synthesized FeN4-SAC, CoN4-SAC, NiN4-SAC, and FeNiN8-DAC along with the N-doped sample and measured their photocatalytic activity toward singlet oxygen ($^1O_2$) generation. We demonstrated that FeN4-SAC has a higher photooxygenation conversion of 86% and a high $^1O_2$ quantum yield of 1.04 (obtained from ESR spectroscopy) in good agreement with our theoretical predictions. Finally, we measured the performance of our synthesized SACs for the two-electron oxygen reduction reaction (ORR), finding a higher $H_2O_2$ production for NiN4-SAC. These results show the advantage of combining DFT calculations, experiments, and data-driven machine learning (ML) techniques as the way forward for the development of single and dual atom photocatalysts.

## ML code availability

Our PySACs ML algorithm is available free of charge at https://github.com/MohsenTamtaji/PySACs.[43] PySACs is applicable for calculating $\Delta G_{H*}$, $\Delta G_{O*}$, $\Delta G_{OOH*}$, $\Delta G_{O*}$, $\Delta G_{OH*}$, $\Delta G_{CO*}$, $\Delta G_{COOH*}$, $\Delta G_{CHO*}$, $\Delta G_{COH*}$, $\eta_{HER}$, $\eta_{ORR}$, $\eta_{OER}$ and $H_{ORR}^{onset}$. It can be used for all transition metal SACs on N- and O-doped graphene- and porphyrin-based substrates. It can be also retrained easily for applications to other materials problems.

## Acknowledgements

Z.L. acknowledge supports by the RGC (16304421), the Innovation and Technology Commission (ITC-CNERC14SC01), Guangdong Science and Technology Department (Project#:2020A0505090003), Research Fund of Guangdong-Hong Kong-Macao Joint Laboratory for Intelligent Micro-Nano Optoelectronic Technology (No. 2020B1212030010), IER foundation (HT-JD-CXY-201907), and Shenzhen Special Fund for Central Guiding the Local Science and Technology Development (2021Szvup136). Technical assistance from the Materials Characterization and Preparation Facilities of HKUST is greatly appreciated. W.A.G. acknowledges support by the DOE Liquid Sunlight Alliance (LiSA) (DE-SC0021266) and the US National Science Foundation (NSF CBET-2005250).

## Associated Content

### Supporting Information

Characterization, photocatalytic activity, bandgap structure through Tauc plot and LEIPS analysis, triplet sensitization from TD-DFT calculations, multi-electron transfer process (Dexter energy transfer, DET) from DFT calculations, and rate of $^1O_2$ sensitization.

### Conflicts of interest

The authors respectfully declare that there are no conflicts of interest to acknowledge for this research.

## References

(1) Wu, Y.; Wu, Q.; Zhang, Q.; Lou, Z.; Liu, K.; Ma, Y.; Wang, Z.; Zheng, Z.; Cheng, H.; Liu, Y.; Dai, Y.; Huang, B.; Wang, P. An Organometal Halide Perovskite Supported Pt Single-Atom Photocatalyst for H 2 Evolution . *Energy Environ. Sci.* **2022**, *15* (3), 1271–1281. https://doi.org/10.1039/d1ee03679c.

(2) Xue, S.; Zhang, T.; Wang, X.; Zhang, Q.; Huang, S.; Zhang, L.; Zhang, L.; Zhu, W.; Wang, Y.; Wu, M.; Zhao, Q.; Li, P.; Wu, W. Cu,Zn Dopants Boost Electron Transfer of Carbon Dots for Antioxidation. *Small* **2021**, *17* (31), 1–11. https://doi.org/10.1002/smll.202102178.

(3) Liu, S.; Tang, N.; Song, T.; Motokura, K.; Shen, Z.; Yang, Y. Coexistence of Fe Nanoclusters Boosting Fe Single Atoms to Generate Singlet Oxygen for E Ffi Cient Aerobic Oxidation of Primary Amines to Imines. **2022**. https://doi.org/10.1021/acscatal.1c04467.

(4) Gu, Y.; Xu, T.; Zhu, Z.; Chen, X.; Chen, W.; Lu, W. Atomic-Scale Tailoring and Molecular-Level Tracking of Oxygen-Containing Tungsten Single-Atom Catalysts with Enhanced Singlet Oxygen Generation. *ACS Appl. Mater. Interfaces* **2021**, 1–10. https://doi.org/10.1021/acsami.1c09016.

(5) Wang, J.; Yin, S.; Zhang, Q.; Cao, F.; Xing, Y.; Zhao, Q.; Wang, Y.; Xu, W.; Wu, W.; Wu, M. Single-Atom Fe-N4 Sites Promote the Triplet-Energy Transfer Process of g-C3N4 for the Photooxidation. *J. Catal.* **2021**, *404*, 89–95. https://doi.org/10.1016/j.jcat.2021.09.010.

(6) Luo, L.; Xiao, X.; Li, Q.; Wang, S.; Li, Y.; Hou, J.; Jiang, B. Engineering of Single Atomic Cu - N 3 Active Sites for E Ffi Cient Singlet Oxygen Production in Photocatalysis. **2021**. https://doi.org/10.1021/acsami.1c17782.

(7) Jie, S.; Yang, C.; Chen, Y.; Liu, Z. Facile Synthesis of Ultra-Stable Co-N-C Catalysts Using Cobalt Porphyrin and Peptides as Precursors for Selective Oxidation of Ethylbenzene. *Mol. Catal.* **2018**, *458* (June), 1–8. https://doi.org/10.1016/j.mcat.2018.08.007.

(8) Jie, S.; Lin, X.; Chen, Q.; Zhu, R.; Zhang, L.; Zhang, B.; Liu, Z. Montmorillonite-Assisted Synthesis of Cobalt-Nitrogen-Doped Carbon Nanosheets for High-Performance Selective Oxidation of Alkyl Aromatics. *Appl. Surf. Sci.* **2018**, *456* (May), 951–958. https://doi.org/10.1016/j.apsusc.2018.06.109.

(9) Yuan, E.; Zhou, M.; Shi, G.; Jian, P.; Hou, X. Atomically Dispersed Co / C 3 N 4 for Boosting Aerobic Cyclohexane Oxidation. 1–42.

(10) Zhou, Y.; Qin, W.; Sun, X.; Zhu, Y.; Niu, J. Synergistic Effects on D-Band Center via Coordination Sites of M-N 3 P 1 ( M = Co and Ni ) in Dual Single Atoms That Enhances Photocatalytic Dechlorination from Tetrachlorobispheonl A. *J. Hazard. Mater.* **2022**, *430* (December 2021), 128419. https://doi.org/10.1016/j.jhazmat.2022.128419.

(11) Ma, X.; Liu, H.; Yang, W.; Mao, G.; Zheng, L.; Jiang, H. L. Modulating Coordination Environment of Single-Atom Catalysts and Their Proximity to Photosensitive Units for Boosting MOF Photocatalysis. *J. Am. Chem. Soc.* **2021**, *143* (31), 12220–12229. https://doi.org/10.1021/jacs.1c05032.

(12) Gao, C.; Chen, S.; Wang, Y.; Wang, J.; Zheng, X.; Zhu, J.; Song, L.; Zhang, W.; Xiong, Y. Heterogeneous Single-Atom Catalyst for Visible-Light-Driven High-Turnover CO2 Reduction: The Role of Electron Transfer. *Adv. Mater.* **2018**, *30* (13). https://doi.org/10.1002/adma.201704624.

(13) Karmodak, N.; Vijay, S.; Kastlunger, G.; Chan, K. Computational Screening of Single and Di-Atom Catalysts for Electrochemical CO 2 Reduction . *ACS Catal.* **2022**, 4818–4824. https://doi.org/10.1021/acscatal.1c05750.

(14) Ma, W.; Mao, J.; He, C.-T.; Shao, L.; Liu, J.; Wang, M.; Yu, P.; Mao, L. Highly Selective Generation of Singlet Oxygen from Dioxygen with Atomically Dispersed Catalysts. *Chem. Sci.* **2022**. https://doi.org/10.1039/d2sc01110g.

(15) Yu, L.; Li, F.; Zhao, J.; Chen, Z. Revisiting Catalytic Performance of Supported Metal Dimers for Oxygen Reduction Reaction via Magnetic Coupling from First Principles. *Adv. Powder Mater.* **2022**, *1* (3), 100031. https://doi.org/10.1016/j.apmate.2022.01.004.

(16) Saha, A.; Gifford, B. J.; He, X.; Ao, G.; Zheng, M.; Kataura, H.; Htoon, H.; Kilina, S.;

Tretiak, S.; Doorn, S. K. Narrow-Band Single-Photon Emission through Selective Aryl Functionalization of Zigzag Carbon Nanotubes. *Nat. Chem.* **2018**, *10* (11), 1089–1095. https://doi.org/10.1038/s41557-018-0126-4.

(17) Wu, W.; Zhang, Q.; Wang, X.; Han, C.; Shao, X.; Wang, Y.; Liu, J.; Li, Z.; Lu, X.; Wu, M. Enhancing Selective Photooxidation through Co−Nx-Doped Carbon Materials as Singlet Oxygen Photosensitizers. *ACS Catal.* **2017**, *7* (10), 7267–7273. https://doi.org/10.1021/acscatal.7b01671.

(18) Liu, D.; He, Q.; Ding, S.; Song, L. Structural Regulation and Support Coupling Effect of Single-Atom Catalysts for Heterogeneous Catalysis. *Advanced Energy Materials*. 2020. https://doi.org/10.1002/aenm.202001482.

(19) Liu, X.; Zheng, L.; Han, C.; Zong, H.; Yang, G.; Lin, S.; Kumar, A.; Jadhav, A. R.; Tran, N. Q.; Hwang, Y.; Lee, J.; Vasimalla, S.; Chen, Z.; Kim, S. G.; Lee, H. Identifying the Activity Origin of a Cobalt Single-Atom Catalyst for Hydrogen Evolution Using Supervised Learning. *Adv. Funct. Mater.* **2021**, *2100547*, 1–9. https://doi.org/10.1002/adfm.202100547.

(20) Wu, L.; Guo, T.; Li, T. Rational Design of Transition Metal Single-Atom Electrocatalysts: A Simulation-Based, Machine Learning-Accelerated Study. *J. Mater. Chem. A* **2020**, *8* (37), 19290–19299. https://doi.org/10.1039/d0ta06207c.

(21) Wang, M.; Zhu, H. Machine Learning for Transition-Metal-Based Hydrogen Generation Electrocatalysts. *ACS Catal.* **2021**, 3930–3937. https://doi.org/10.1021/acscatal.1c00178.

(22) Chen, L.; Xu, X.; Yang, W.; Jia, J. Recent Advances in Carbon-Based Electrocatalysts for Oxygen Reduction Reaction. *Chinese Chem. Lett.* **2020**, *31* (3), 626–634. https://doi.org/10.1016/j.cclet.2019.08.008.

(23) Johnson, D.; Qiao, Z.; Djire, A. Progress and Challenges of Carbon Dioxide Reduction Reaction on Transition Metal Based Electrocatalysts. **2021**. https://doi.org/10.1021/acsaem.1c01624.

(24) Huang, Y.; Rehman, F.; Tamtaji, M.; Li, X.; Huang, Y.; Zhang, T.; Luo, Z. Mechanistic Understanding and Design of Non-Noble Metal-Based Single-Atom Catalysts Supported

on Two-Dimensional Materials for CO2 Electroreduction. *J. Mater. Chem. A* **2021**.

(25) Deng, C.; Su, Y.; Li, F.; Shen, W.; Chen, Z.; Tang, Q. Understanding Activity Origin for the Oxygen Reduction Reaction on Bi-Atom Catalysts by DFT Studies and Machine-Learning. *J. Mater. Chem. A* **2020**, *8* (46), 24563–24571. https://doi.org/10.1039/d0ta08004g.

(26) Yuan, H.; Li, Z.; Zeng, X. C.; Yang, J. Descriptor-Based Design Principle for Two-Dimensional Single-Atom Catalysts: Carbon Dioxide Electroreduction. *J. Phys. Chem. Lett.* **2020**, *11* (9), 3481–3487. https://doi.org/10.1021/acs.jpclett.0c00676.

(27) Sun, X.; Zheng, J.; Gao, Y.; Qiu, C.; Yan, Y.; Yao, Z.; Deng, S.; Wang, J. Machine-Learning-Accelerated Screening of Hydrogen Evolution Catalysts in MBenes Materials. *Appl. Surf. Sci.* **2020**, *526* (February), 146522. https://doi.org/10.1016/j.apsusc.2020.146522.

(28) Hummers, W. S.; Offeman, R. E. Preparation of Graphitic Oxide. *J. Am. Chem. Soc.* **1958**, *80* (6), 1339. https://doi.org/10.1021/ja01539a017.

(29) Hossain, M. D.; Liu, Z.; Zhuang, M.; Yan, X.; Xu, G. L.; Gadre, C. A.; Tyagi, A.; Abidi, I. H.; Sun, C. J.; Wong, H.; Guda, A.; Hao, Y.; Pan, X.; Amine, K.; Luo, Z. Rational Design of Graphene-Supported Single Atom Catalysts for Hydrogen Evolution Reaction. *Advanced Energy Materials*. 2019. https://doi.org/10.1002/aenm.201803689.

(30) Khan, K.; Liu, T.; Arif, M.; Yan, X.; Hossain, M. D.; Rehman, F.; Zhou, S.; Yang, J.; Sun, C.; Bae, S. H.; Kim, J.; Amine, K.; Pan, X.; Luo, Z. Laser-Irradiated Holey Graphene-Supported Single-Atom Catalyst towards Hydrogen Evolution and Oxygen Reduction. *Adv. Energy Mater.* **2021**, *2101619*, 1–9. https://doi.org/10.1002/aenm.202101619.

(31) Hai, X.; Xi, S.; Mitchell, S.; Harrath, K.; Xu, H.; Akl, D. F.; Kong, D.; Li, J.; Li, Z.; Sun, T.; Yang, H.; Cui, Y.; Su, C.; Zhao, X.; Li, J.; Pérez-ramírez, J.; Lu, J. Scalable Two-Step Annealing Method for Preparing Ultra-High-Density Single-Atom Catalyst Libraries. https://doi.org/10.1038/s41565-021-01022-y.

(32) Gómez-Bombarelli, R.; Aguilera-Iparraguirre, J.; Hirzel, T. D.; Duvenaud, D.; Maclaurin, D.; Blood-Forsythe, M. A.; Chae, H. S.; Einzinger, M.; Ha, D. G.; Wu, T.; Markopoulos,

G.; Jeon, S.; Kang, H.; Miyazaki, H.; Numata, M.; Kim, S.; Huang, W.; Hong, S. I.; Baldo, M.; Adams, R. P.; Aspuru-Guzik, A. Design of Efficient Molecular Organic Light-Emitting Diodes by a High-Throughput Virtual Screening and Experimental Approach. *Nat. Mater.* **2016**, *15* (10), 1120–1127. https://doi.org/10.1038/nmat4717.

(33) De Queiroz, T. B.; De Figueroa, E. R.; Coutinho-Neto, M. D.; Maciel, C. D.; Tapavicza, E.; Hashemi, Z.; Leppert, L. First Principles Theoretical Spectroscopy of Methylene Blue: Between Limitations of Time-Dependent Density Functional Theory Approximations and Its Realistic Description in the Solvent. *J. Chem. Phys.* **2021**, *154* (4). https://doi.org/10.1063/5.0029727.

(34) Nwahara, N.; Motaung, M.; Abrahams, G.; Mashazi, P.; Mack, J.; Prinsloo, E.; Nyokong, T. Dual Singlet Oxygen and Nitric Oxide-Releasing Silicon Phthalocyanine for Augmented Photodynamic Therapy. *Mater. Today Chem.* **2022**, *26*, 101201. https://doi.org/10.1016/j.mtchem.2022.101201.

(35) Gu, W.; Wang, X.; Wen, J.; Cao, S.; Jiao, L.; Wu, Y.; Wei, X.; Zheng, L.; Hu, L.; Zhang, L.; Zhu, C. Modulating Oxygen Reduction Behaviors on Nickel Single-Atom Catalysts to Probe the Electrochemiluminescence Mechanism at the Atomic Level. *Anal. Chem.* **2021**, *93* (24), 8663–8670. https://doi.org/10.1021/acs.analchem.1c01835.

(36) Nayyar, I. H.; Masunov, A. E.; Tretiak, S. Comparison of TD-DFT Methods for the Calculation of Two-Photon Absorption Spectra of Oligophenylvinylenes. *J. Phys. Chem. C* **2013**, *117* (35), 18170–18189. https://doi.org/10.1021/jp403981d.

(37) Urrego-Ortiz, R.; Builes, S.; Calle-Vallejo, F. Impact of Intrinsic Density Functional Theory Errors on the Predictive Power of Nitrogen Cycle Electrocatalysis Models. *ACS Catal.* **2022**, 4784–4791. https://doi.org/10.1021/acscatal.1c05333.

(38) Patel, A. M.; Ringe, S.; Siahrostami, S.; Bajdich, M.; Nørskov, J. K.; Kulkarni, A. R. Theoretical Approaches to Describing the Oxygen Reduction Reaction Activity of Single-Atom Catalysts. *J. Phys. Chem. C* **2018**, *122* (51), 29307–29318. https://doi.org/10.1021/acs.jpcc.8b09430.

(39) Tirado-Rives, J.; Jorgensen, W. L. Performance of B3LYP Density Functional Methods

for a Large Set of Organic Molecules. *J. Chem. Theory Comput.* **2008**, *4* (2), 297–306. https://doi.org/10.1021/ct700248k.

(40) Zhou, L.; Martirez, J. M. P.; Finzel, J.; Zhang, C.; Swearer, D. F.; Tian, S.; Robatjazi, H.; Lou, M.; Dong, L.; Henderson, L.; Christopher, P.; Carter, E. A.; Nordlander, P.; Halas, N. J. Light-Driven Methane Dry Reforming with Single Atomic Site Antenna-Reactor Plasmonic Photocatalysts. *Nat. Energy* **2020**, *5* (1), 61–70. https://doi.org/10.1038/s41560-019-0517-9.

(41) Badran, H. M.; Eid, K. M.; Ammar, H. Y. DFT and TD-DFT Studies of Halogens Adsorption on Cobalt-Doped Porphyrin: Effect of the External Electric Field. *Results Phys.* **2021**, *23*, 103964. https://doi.org/10.1016/j.rinp.2021.103964.

(42) Lu, T.; Chen, F. Multiwfn: A Multifunctional Wavefunction Analyzer. *J. Comput. Chem.* **2012**, *33* (5), 580–592. https://doi.org/10.1002/jcc.22885.

(43) Tamtaji, M. PySACs https://github.com/MohsenTamtaji/PySACs.

(44) Tamtaji, M.; Tyagi, A.; You, C. Y.; Galligan, P. R.; Liu, H.; Liu, Z.; Karimi, R.; Cai, Y.; Roxas, A. P.; Wong, H.; Luo, Z. Singlet Oxygen Photosensitization Using Graphene-Based Structures and Immobilized Dyes : A Review. *ACS Appl. Nano Mater.* **2021**, *4* (5), 7563–7583. https://doi.org/10.1021/acsanm.1c01436.

(45) Ge, J.; Lan, M.; Zhou, B.; Liu, W.; Guo, L.; Wang, H.; Jia, Q.; Niu, G.; Huang, X.; Zhou, H.; Meng, X.; Wang, P.; Lee, C. S.; Zhang, W.; Han, X. A Graphene Quantum Dot Photodynamic Therapy Agent with High Singlet Oxygen Generation. *Nat. Commun.* **2014**, *5*, 1–8. https://doi.org/10.1038/ncomms5596.

(46) Tabachnyk, M.; Ehrler, B.; Gélinas, S.; Böhm, M. L.; Walker, B. J.; Musselman, K. P.; Greenham, N. C.; Friend, R. H.; Rao, A. Resonant Energy Transfer of Triplet Excitons from Pentacene to PbSe Nanocrystals. *Nat. Mater.* **2014**, *13* (11), 1033–1038. https://doi.org/10.1038/NMAT4093.

(47) Zhang, Y.; Zhao, J.; Wang, H.; Xiao, B.; Zhang, W.; Zhao, X.; Lv, T.; Thangamuthu, M.; Zhang, J.; Guo, Y.; Ma, J.; Lin, L.; Tang, J.; Huang, R.; Liu, Q. Single-Atom Cu Anchored Catalysts for Photocatalytic Renewable H2 Production with a Quantum

Efficiency of 56%. *Nat. Commun.* **2022**, *13* (1). https://doi.org/10.1038/s41467-021-27698-3.

(48) Cheng, S.; Sun, Z.; Lim, K. H.; Gani, T. Z. H.; Zhang, T.; Wang, Y.; Yin, H.; Liu, K.; Guo, H.; Du, T.; Liu, L.; Li, G. K.; Yin, Z.; Kawi, S. Emerging Strategies for CO 2 Photoreduction to CH 4 : From Experimental to Data-Driven Design . *Adv. Energy Mater.* **2022**, *2200389*, 2200389. https://doi.org/10.1002/aenm.202200389.

(49) Wang, X.; Pan, H.; Sun, M.; Zhang, Y. Au Single Atom-Anchored WO 3 /TiO 2 Nanotubes for the Photocatalytic Degradation of Volatile Organic Compounds . *J. Mater. Chem. A* **2022**, *10* (11), 6078–6085. https://doi.org/10.1039/d1ta08143h.

(50) Xia, B.; Zhang, Y.; Ran, J.; Jaroniec, M.; Qiao, S. Z. Single-Atom Photocatalysts for Emerging Reactions. *ACS Cent. Sci.* **2021**, *7* (1), 39–54. https://doi.org/10.1021/acscentsci.0c01466.

(51) He, J.; Liu, P.; Ran, R.; Wang, W.; Zhou, W.; Shao, Z. Single-Atom Catalysts for High-Efficiency Photocatalytic and Photoelectrochemical Water Splitting: Distinctive Roles, Unique Fabrication Methods and Specific Design Strategies. *J. Mater. Chem. A* **2022**, *10* (13), 6835–6871. https://doi.org/10.1039/d2ta00835a.

(52) Yan, B.; Song, H.; Yang, G. A Facile and Green Large-Scale Fabrication of Single Atom Catalysts for High Photocatalytic H2 Evolution Activity. *Chem. Eng. J.* **2022**, *427* (August 2021), 131795. https://doi.org/10.1016/j.cej.2021.131795.

(53) Yang, G.; Zhu, J.; Yuan, P.; Hu, Y.; Qu, G.; Lu, B. A.; Xue, X.; Yin, H.; Cheng, W.; Cheng, J.; Xu, W.; Li, J.; Hu, J.; Mu, S.; Zhang, J. N. Regulating Fe-Spin State by Atomically Dispersed Mn-N in Fe-N-C Catalysts with High Oxygen Reduction Activity. *Nat. Commun.* **2021**, *12* (1), 4–13. https://doi.org/10.1038/s41467-021-21919-5.

(54) Jiao, L.; Zhu, J.; Zhang, Y.; Yang, W.; Zhou, S.; Li, A.; Xie, C.; Zheng, X.; Zhou, W.; Yu, S.; Jiang, H. Non-Bonding Interaction of Neighboring Fe and Ni Single-Atom Pairs on MOF-Derived N‐Doped Carbon for Enhanced CO 2 Electroreduction. **2021**. https://doi.org/10.1021/jacs.1c08050.

(55) Yang, H. Bin; Hung, S. F.; Liu, S.; Yuan, K.; Miao, S.; Zhang, L.; Huang, X.; Wang, H.

Y.; Cai, W.; Chen, R.; Gao, J.; Yang, X.; Chen, W.; Huang, Y.; Chen, H. M.; Li, C. M.; Zhang, T.; Liu, B. Atomically Dispersed Ni(i) as the Active Site for Electrochemical CO2 Reduction. *Nat. Energy* **2018**, *3* (2), 140–147. https://doi.org/10.1038/s41560-017-0078-8.

(56) Li, X.; Cao, C. S.; Hung, S. F.; Lu, Y. R.; Cai, W.; Rykov, A. I.; Miao, S.; Xi, S.; Yang, H.; Hu, Z.; Wang, J.; Zhao, J.; Alp, E. E.; Xu, W.; Chan, T. S.; Chen, H.; Xiong, Q.; Xiao, H.; Huang, Y.; Li, J.; Zhang, T.; Liu, B. Identification of the Electronic and Structural Dynamics of Catalytic Centers in Single-Fe-Atom Material. *Chem* **2020**, *6* (12), 3440–3454. https://doi.org/10.1016/j.chempr.2020.10.027.

(57) Khan, K.; Yan, X.; Yu, Q.; Bae, S. H.; White, J. J.; Liu, J.; Liu, T.; Sun, C.; Kim, J.; Cheng, H. M.; Wang, Y.; Liu, B.; Amine, K.; Pan, X.; Luo, Z. Stone-Wales Defect-Rich Carbon-Supported Dual-Metal Single Atom Sites for Zn-Air Batteries. *Nano Energy* **2021**, *90* (PA), 106488. https://doi.org/10.1016/j.nanoen.2021.106488.

(58) Hossain, M. D.; Liu, Z.; Zhuang, M.; Yan, X.; Xu, G. L.; Gadre, C. A.; Tyagi, A.; Abidi, I. H.; Sun, C. J.; Wong, H.; Guda, A.; Hao, Y.; Pan, X.; Amine, K.; Luo, Z. Rational Design of Graphene-Supported Single Atom Catalysts for Hydrogen Evolution Reaction. *Adv. Energy Mater.* **2019**, *9* (10), 1–10. https://doi.org/10.1002/aenm.201803689.

(59) Eckmann, A.; Felten, A.; Verzhbitskiy, I.; Davey, R.; Casiraghi, C. Raman Study on Defective Graphene: Effect of the Excitation Energy, Type, and Amount of Defects. *Phys. Rev. B - Condens. Matter Mater. Phys.* **2013**, *88* (3), 1–11. https://doi.org/10.1103/PhysRevB.88.035426.

(60) Gong, Y. N.; Zhong, W.; Li, Y.; Qiu, Y.; Zheng, L.; Jiang, J.; Jiang, H. L. Regulating Photocatalysis by Spin-State Manipulation of Cobalt in Covalent Organic Frameworks. *J. Am. Chem. Soc.* **2020**, *142* (39), 16723–16731. https://doi.org/10.1021/jacs.0c07206.

(61) Di Liberto, G.; Cipriano, L. A.; Tosoni, S.; Pacchioni, G. Rational Design of Semiconductor Heterojunctions for Photocatalysis. *Chem. - A Eur. J.* **2021**, *27* (53), 13306–13317. https://doi.org/10.1002/chem.202101764.

(62) Hamad, S.; Hernandez, N. C.; Aziz, A.; Ruiz-Salvador, A. R.; Calero, S.; Grau-Crespo, R. Electronic Structure of Porphyrin-Based Metal-Organic Frameworks and Their Suitability

for Solar Fuel Production Photocatalysis. *J. Mater. Chem. A* **2015**, *3* (46), 23458–23465. https://doi.org/10.1039/c5ta06982c.

(63) Conboy, G.; Spencer, H. J.; Angioni, E.; Kanibolotsky, A. L.; Findlay, N. J.; Coles, S. J.; Wilson, C.; Pitak, M. B.; Risko, C.; Coropceanu, V.; Brédas, J. L.; Skabara, P. J. To Bend or Not to Bend-Are Heteroatom Interactions within Conjugated Molecules Effective in Dictating Conformation and Planarity? *Mater. Horizons* **2016**, *3* (4), 333–339. https://doi.org/10.1039/c6mh00051g.

(64) Zou, Y.; Abednatanzi, S.; Gohari Derakhshandeh, P.; Mazzanti, S.; Schüßlbauer, C. M.; Cruz, D.; Van Der Voort, P.; Shi, J.-W.; Antonietti, M.; Guldi, D. M.; Savateev, A. Red Edge Effect and Chromoselective Photocatalysis with Amorphous Covalent Triazine-Based Frameworks. *Nat. Commun.* **2022**, *13* (1), 1–13. https://doi.org/10.1038/s41467-022-29781-9.

(65) Gaul, C.; Hutsch, S.; Schwarze, M.; Schellhammer, K. S.; Bussolotti, F.; Kera, S.; Cuniberti, G.; Leo, K.; Ortmann, F. Insight into Doping Efficiency of Organic Semiconductors from the Analysis of the Density of States in N-Doped. *Nat. Mater.* **2018**, *17* (5), 439–444. https://doi.org/10.1038/s41563-018-0030-8.

(66) Terashima, M.; Miyayama, T.; Shirao, T.; Mo, H. W.; Hatae, Y.; Fujimoto, H.; Watanabe, K. The Electronic Band Structure Analysis of OLED Device by Means of in Situ LEIPS and UPS Combined with GCIB. *Surf. Interface Anal.* **2020**, *52* (12), 948–952. https://doi.org/10.1002/sia.6777.

(67) Zhao, S.; Zhao, X. Insights into the Role of Singlet Oxygen in the Photocatalytic Hydrogen Peroxide Production over Polyoxometalates-Derived Metal Oxides Incorporated into Graphitic Carbon Nitride Framework. *Appl. Catal. B Environ.* **2019**, *250* (November 2018), 408–418. https://doi.org/10.1016/j.apcatb.2019.02.031.

(68) Teng, Z.; Cai, W.; Sim, W.; Zhang, Q.; Wang, C.; Su, C.; Ohno, T. Photoexcited Single Metal Atom Catalysts for Heterogeneous Photocatalytic H2O2 Production: Pragmatic Guidelines for Predicting Charge Separation. *Appl. Catal. B Environ.* **2021**, *282* (September 2020), 119589. https://doi.org/10.1016/j.apcatb.2020.119589.

(69) Chu, C.; Zhu, Q.; Pan, Z.; Gupta, S.; Huang, D.; Du, Y.; Weon, S.; Wu, Y.; Muhich, C.; Stavitski, E.; Domen, K.; Kim, J. H. Spatially Separating Redox Centers on 2D Carbon Nitride with Cobalt Single Atom for Photocatalytic H2O2 Production. *Proc. Natl. Acad. Sci. U. S. A.* **2020**, *117* (12), 6376–6382. https://doi.org/10.1073/pnas.1913403117.

(70) Sun, Y.; Han, L.; Strasser, P. A Comparative Perspective of Electrochemical and Photochemical Approaches for Catalytic H2O2production. *Chem. Soc. Rev.* **2020**, *49* (18), 6605–6631. https://doi.org/10.1039/d0cs00458h.

(71) Xue, Z. H.; Luan, D.; Zhang, H.; (David) Lou, X. W. Single-Atom Catalysts for Photocatalytic Energy Conversion. *Joule* **2022**, *6* (1), 92–133. https://doi.org/10.1016/j.joule.2021.12.011.

(72) Song, H.; Wei, L.; Chen, C.; Wen, C.; Han, F. Photocatalytic Production of H2O2 and Its in Situ Utilization over Atomic-Scale Au Modified MoS2 Nanosheets. *J. Catal.* **2019**, *376*, 198–208. https://doi.org/10.1016/j.jcat.2019.06.015.

(73) Sheng, B.; Deng, C.; Li, Y.; Xie, S.; Wang, Z.; Sheng, H.; Zhao, J. In Situ Hydroxylation of a Single-Atom Iron Catalyst for Preferential 1O2Production from H2O2. *ACS Catal.* **2022**, 14679–14688. https://doi.org/10.1021/acscatal.2c04484.

(74) Jiang, K.; Back, S.; Akey, A. J.; Xia, C.; Hu, Y.; Liang, W.; Schaak, D.; Stavitski, E.; Nørskov, J. K.; Siahrostami, S.; Wang, H. Highly Selective Oxygen Reduction to Hydrogen Peroxide on Transition Metal Single Atom Coordination. *Nat. Commun.* **2019**, *10* (1). https://doi.org/10.1038/s41467-019-11992-2.

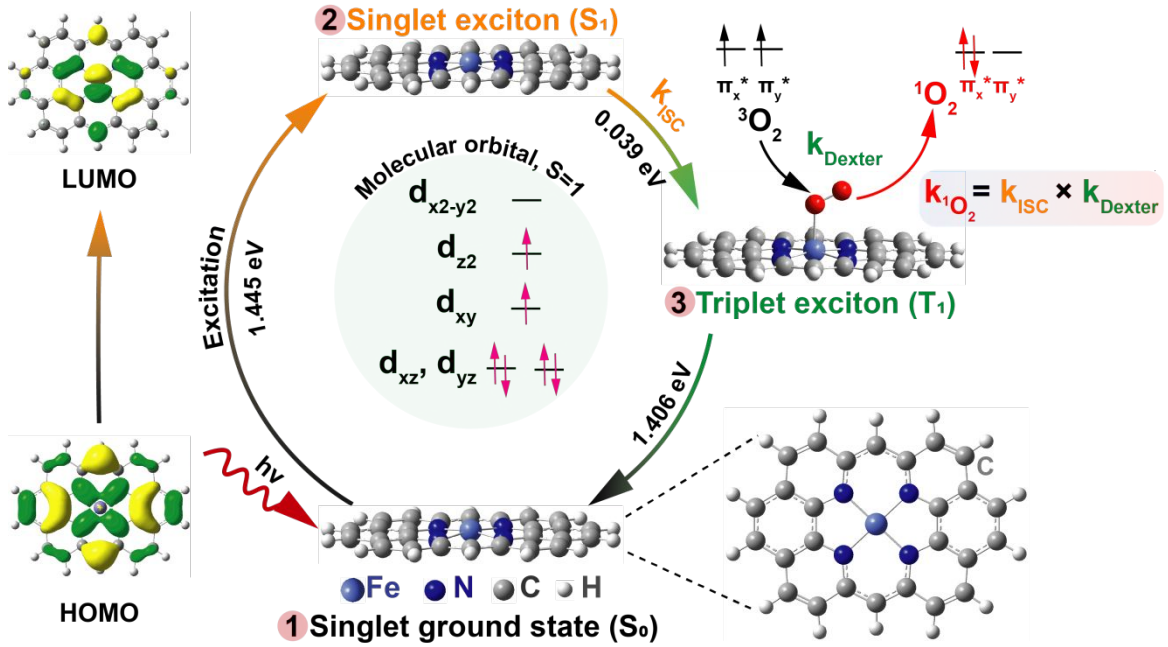


**Scheme 1.** Schematic Jablonski diagram for the application of SACs to $^1O_2$ sensitization indicating the singlet ($S_1$) and triplet ($T_1$) excitons based on ground-state ($S_0$) geometry. This suggests a synergistic effect for intersystem crossing (ISC) and Dexter energy transfers.

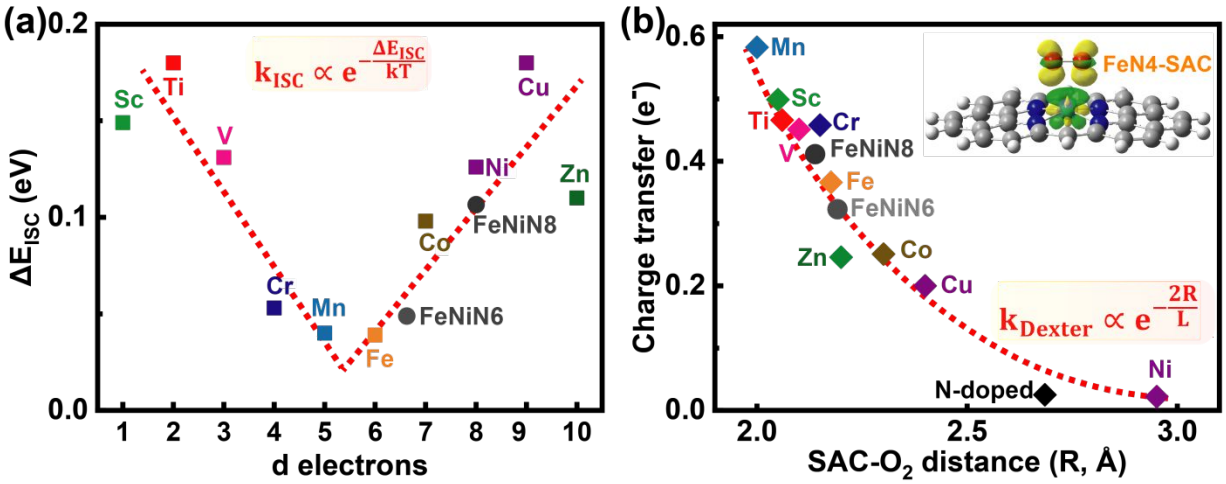


**Figure 1. TD-DFT and DFT calculations.** (a) Volcano plot for intersystem crossing energy gap ($\Delta E_{ISC}$) versus the electrons in d orbital of 3d transition metals, showing that the lowest value corresponds to FeN4-SAC. (b) The Bader charge transfer as a function of the distance between SACs and $O_2$ obtained from DFT calculations. This shows that the highest and lowest charge transfers correspond to MnN4-SAC and NiN4-SAC, respectively. The inset shows the charge transfer from FeN4-SAC to $O_2$ during adsorption. Yellow and green colors represent electron availability and deficiency, respectively, with the Isosurface value of 0.0048 e/Å$^3$.

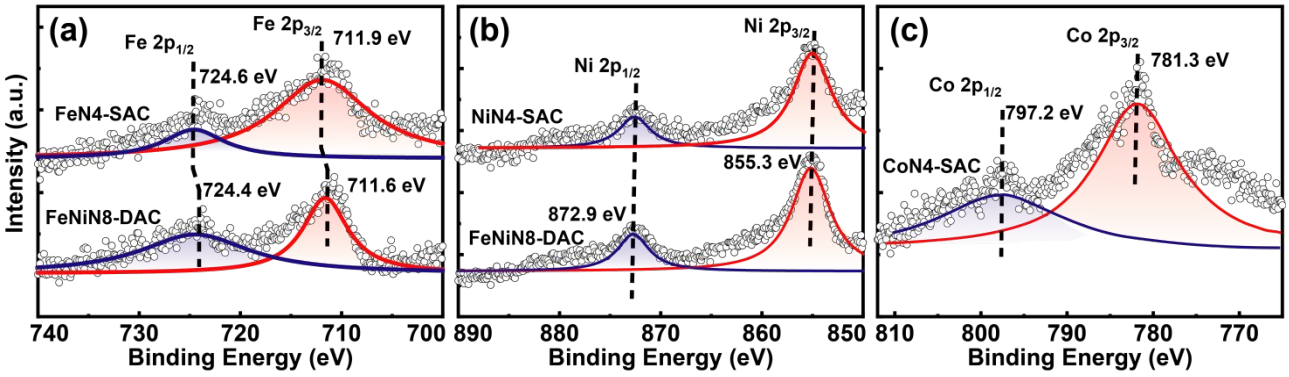


**Figure 2. XPS characterization.** (a) The Fe 2p, (b) Ni 2p, and (c) Co 2p XPS spectra of synthesized samples, showing two peaks belonging to 2p3/2 and 2p1/2. The binding energy of Fe $2p_{3/2}$ in FeNiN8-DAC shifts by -0.3 eV compared with that in FeN4-SAC, suggesting a higher valence oxidation state for Fe, while there is no shift in the Ni $2p_{3/2}$.

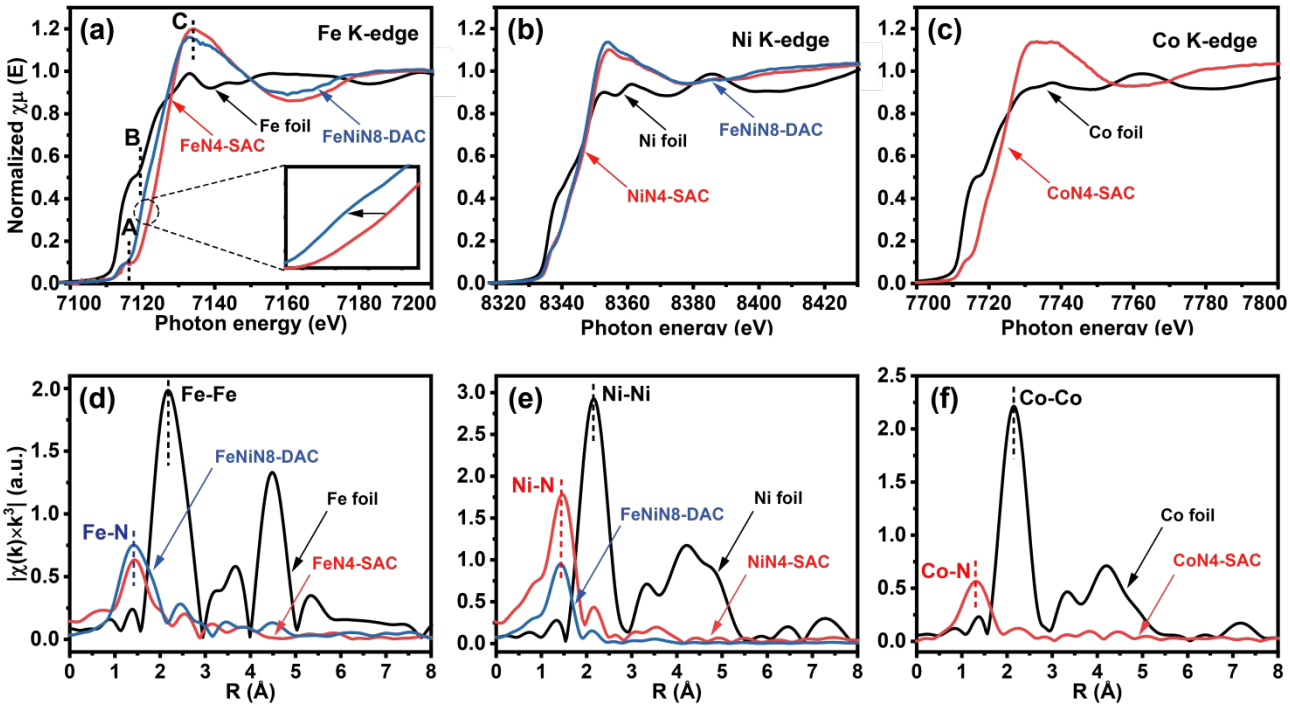


**Figure 3. XANES and EXAFS characterizations.** (a) Fe K-edge, (b) Ni K-edge, and (c) Co K-edge XANES spectra of our synthesized samples and their reference bulk samples. Three peaks are identified with A, B, and C representing 1s→3d, 1s→$4p_z$, 1s→$4p_{xy}$ transitions, and multiple scattering.[30] Fourier transformations (FT) EXAFS spectra in R space of (d) of Fe, (e) Ni, and (f) Co with their reference bulk samples. The primary peaks attributed to Fe-, Co-, and Ni-N are different from Fe-Fe, Co-Co, and Ni-Ni peaks, respectively.

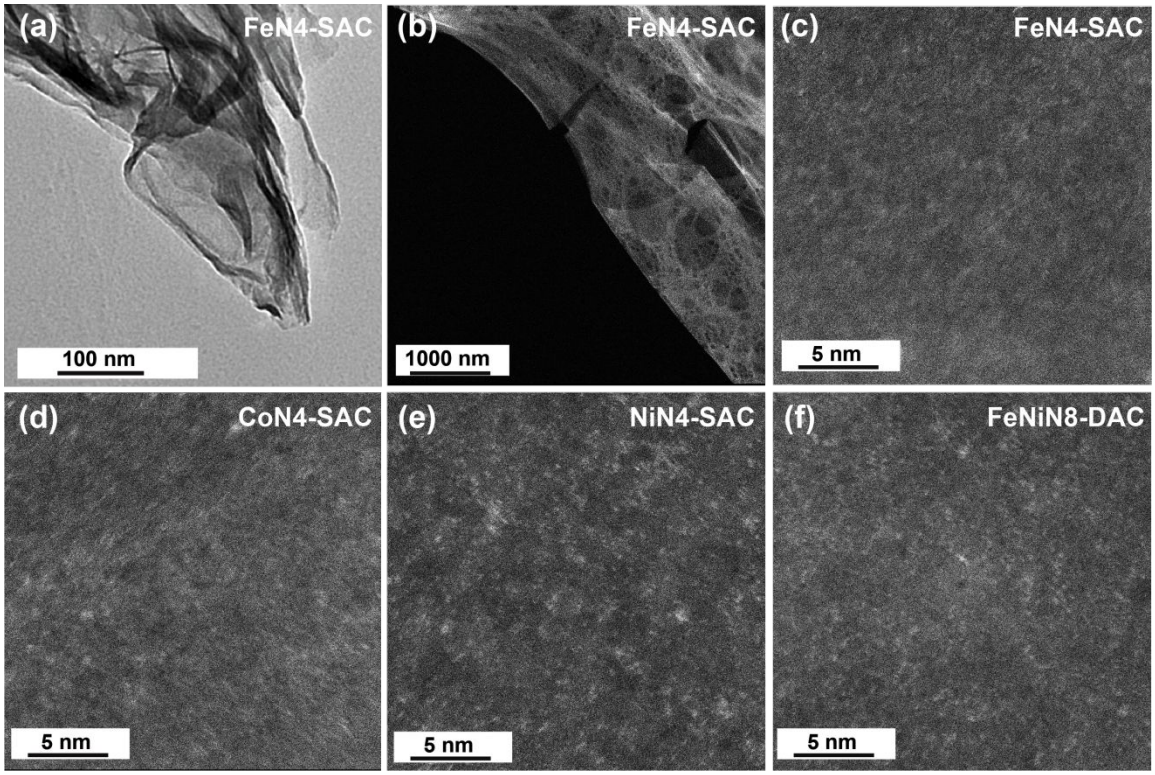


**Figure 4. Structure characterization**. (a, b) TEM and STEM images of the FeN4-SAC sample, showing its porous structure. (c-f) STEM images of FeN4-SAC, CoN4-SAC, NiN4-SAC, and FeNiN8-DAC, showing that the metal atoms are atomically dispersed on the graphene support.

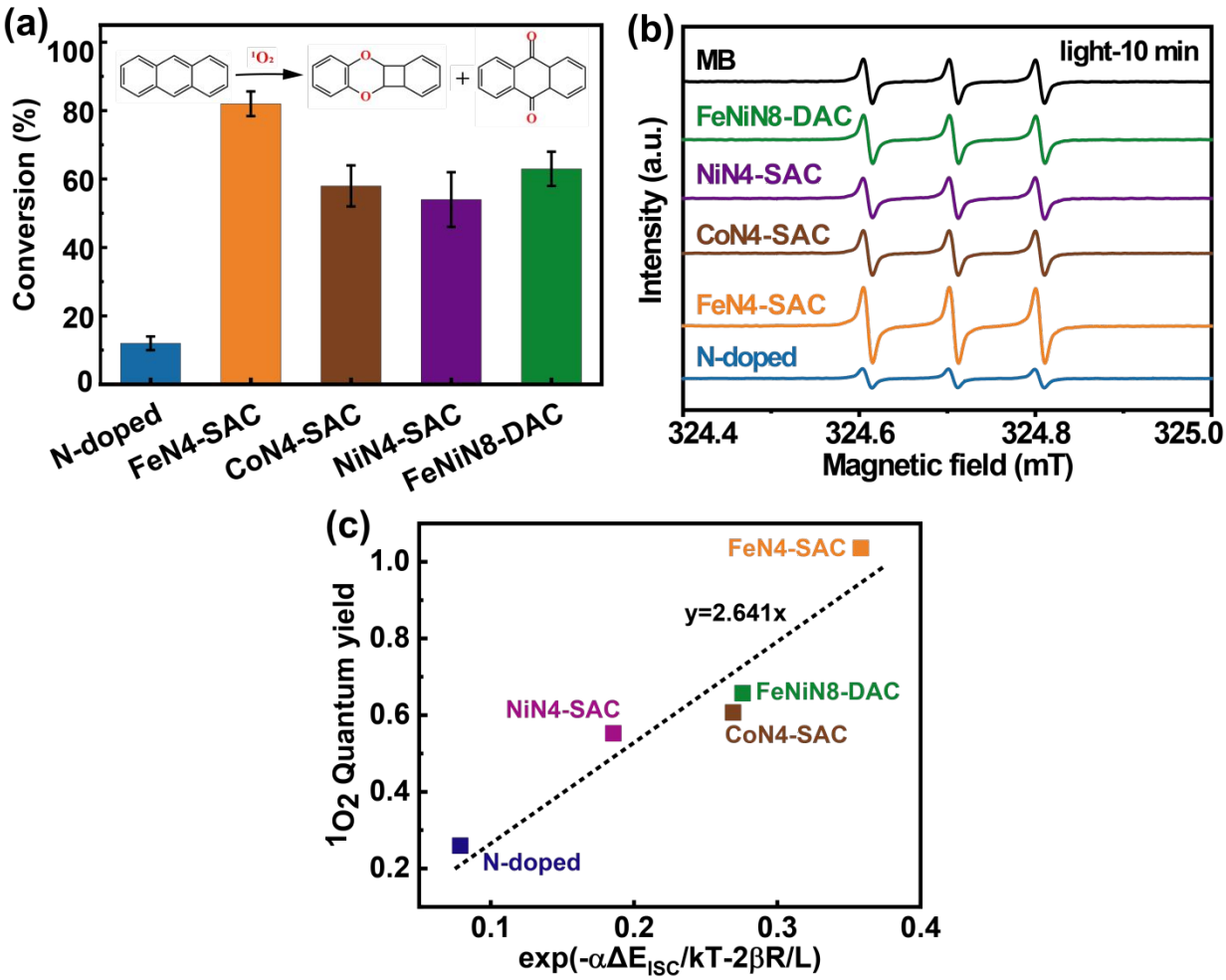


**Figure 5. Photocatalytic activity.** (a) Reaction conversion for photooxygenation of anthracene and for $^1O_2$ quantum yields of the synthesized samples. The inset shows a schematic for the photooxygenation of anthracene. (b) ESR spectra of synthesized samples upon irradiation for 10 min in the presence of TEMP. (c) Calculated $^1O_2$ quantum yield from ESR results versus exp(-$\alpha\Delta E_{ISC}$/kT-2βR/L), indicating the synergistic effect of ISC and Dexter energy transfers leading to a high $^1O_2$ quantum yield for FeN4-SAC.

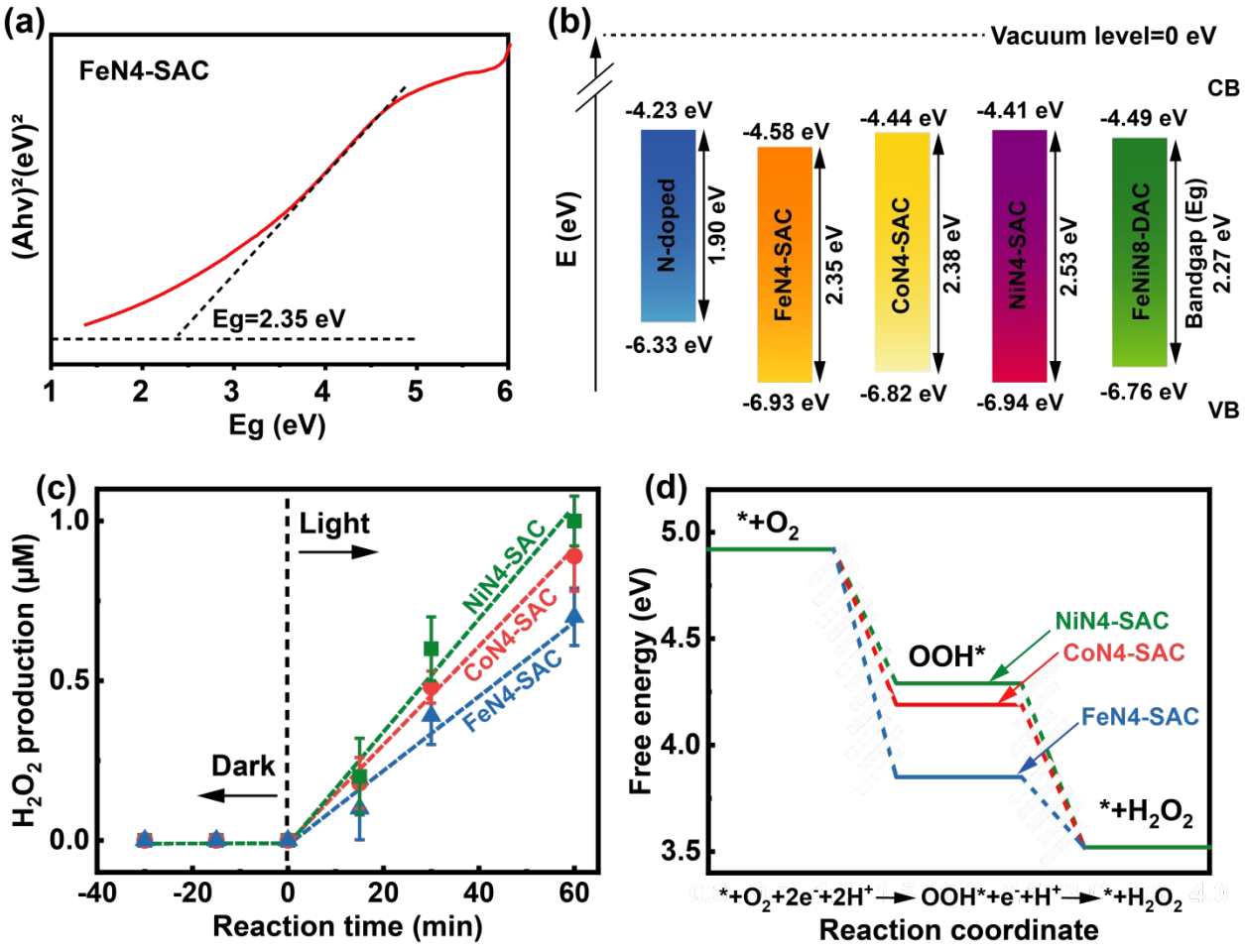


**Figure 6. Bandgap structure and two-electron oxygen reduction reaction (ORR).** (a) Tauc plot of FeN4-SAC sample. (b) Predicted Bandgaps of synthesized samples with respect to the vacuum level, indicating the lower electron-hole recombination for NiN4-SAC. (c) Photocatalytic $H_2O_2$ production over time. (d) Free energy diagram of the two-electron ORR on SACs, obtained from machine learning (ML). Increased $H_2O_2$ production for NiN4-SAC is due to its larger bandgap and its higher Gibbs free energy of OOH* intermediate ($\Delta G_{OOH*}$).